Application of Equivalent Edge Currents to Correct the Backscattered Physical Optics Field of Flat Plates

V. Stein

Institute for Radio Frequency Technology
German Aerospace Research Establishment
D-8031 Oberpfaffenhofen

Abstract

In the microwave case the physical optics (PO) method is frequently used for the analysis of complex structures which are modeled by flat plates of triangular or quadrangular shape. The study of the radar cross section (RCS) of an isolated panel, however, reveals deviations from experimental results which are due to edge diffraction effects not considered by PO. In order to correct the PO-field by an additive field term, the equivalent fringe currents (EC) of Michaeli have been used to derive the backscattering matrix of an isolated edge. By adding the matrices of the individual edges to the PO-matrix the RCS of a square flat plate with zero and finite thickness is analysed and the result is compared with measurements. The efficiency of the method is demonstrated for objects modeled by a higher number of panels and edges, namely a cylinder and a double dihedral. All computations were performed with the computer code SIG5 of the Institute.

1. Introduction

Since several years, the computer program SIG5 is applied in the Institute for Radio Frequency Technology for the prediction of the RCS of structures which are complicated in shape and large compared to the wavelength. SIG5, based on PO, is capable of analysing perfectly and imperfectly conducting structures, including double reflections. The targets are modeled by panels of triangular and quadrangular shape, see Fig. 1.1. The hidden surface problem inherent with PO is solved by an exact construction of the shadow boundary for each panel, whose size is only limited by the admissible deviation between the true surface and the model surface. SIG5 is organized in a very similar way to the computer code RECOTA, developed by the Boeing Aerospace Company, Seattle [1]. SIG5 has been successfully tested for a series of perfectly conducting basic structures such as a sphere, cylinder, cube, circular disk and a double dihedral [2-4]. Also, more complex bodies like a periscope structure have been analysed with promising results [5].

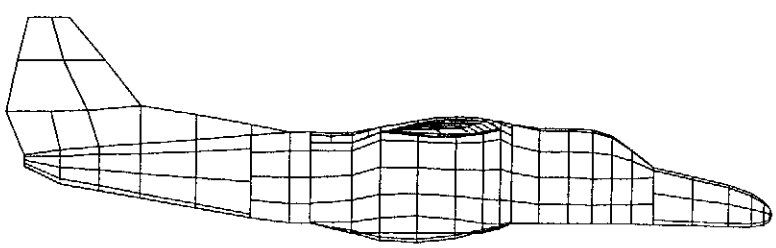

Fig. 1.1
Panel model of an airplane for the application of PO.

Despite the good results which are generally available with PO, there are special cases (certain structures, specific pattern cuts, selected polarizations) where deviations of practical significance between computational and experimental results are observed. They frequently can be explained by the feature of PO to treat the influence of an edge only as the geometrical boundary of a panel thus neglecting physical edge diffraction effects.

The choice of a theory which takes into account edge diffraction effects is influenced by the following viewpoints:

a) Since SIG5 is a very comprehensive computer code each extension should cause a minimum of changes. Therefore, theories are preferred which are able to correct the PO-solution by an additive term.

b) In computing the RCS of large and complex objects modeled by numerous panels the computer effort increases considerably. Therefore, theories which need a high computer effort are not favoured.

c) Since edges of arbitrary length, wedge angle and orientation in space occur in the target model, the theory should not present a solution for a specific panel, rather, the diffracted field of an isolated edge must be described by the specific edge parameters alone.

Bearing these points in mind, only asymptotic theories come into question, which either describe the difference between the total wedge diffracted field and the PO-field directly [6,7] or which evaluate fringe currents flowing along the edge and generating the same difference field by evaluating the radiation integral over the length of the edge [8, 9].

In this paper, the second theory is followed. Here the fringe currents given in [9] are preferred, since they are valid for arbitrary aspects of observation. On the basis of these currents, the backscattering matrix for an isolated edge is derived.

In the following section the theoretical background is discussed. In section 3, the theory is applied for the RCS-analysis of a panel. In section 4, the results for a cylinder and a double dihedral are presented. Section 5, finally, summarizes some conclusions on the basis of the preceeding analysis.

2. Theoretical Background

The results of the theories used in the computer code SIG5 are expressed by the backscattering matrix

$$(2.1) \qquad [T] = \begin{bmatrix} t_{11} & t_{12} \\ t_{21} & t_{22} \end{bmatrix} ,$$

which relates the cartesian components of the scattered field $\vec{E}_s$ to those of the incident field $\vec{E}_e$:

$$(2.2) \qquad \begin{bmatrix} E_{sx} \\ E_{sy} \end{bmatrix} = [T] \begin{bmatrix} E_{ex} \\ E_{ey} \end{bmatrix} .$$

The propagation direction of the scattered field is given by the z-axis (observer fixed coordinate system). From the complex elements t_{ij} of the scattering matrix the polarization dependent RCS is computed:

$$(2.3) \qquad \sigma_{ij} = \lim_{r\to\infty} (4\pi r^2\, t_{ij}\, t_{ij}^{*}) \ ,$$

where r is the distance between the radar observer and the test object. The RCS referred to 1 square meter and expressed in decibels yields the quantity dBsm, which is used in this paper to compare theoretical and experimental results for the selected transmitting/receiving polarizations.

The total scattering matrix [T] of a complex body can be thought to be composed of a matrix $[T^{PO}]$ which is the sum of the scattering matrices based on PO of the individual N panels and the scattering matrix $[T^{f}]$ which sums up the scattering matrices of the M edges of all panels:

$$(2.4) \qquad [T] = [T^{PO}] + [T^{f}] \ , \quad [T^{PO}] = \sum_{n}^{N} [T_n^{PO}] \ , \quad [T^{f}] = \sum_{m}^{M} [T_m^{f}] \ .$$

The PO-scattering matrix of an individual panel of zero thickness and perfect conductivity is readily evaluated using the radiation integral

$$(2.5) \qquad \vec{E}_s(\vec{r}) = \frac{jk}{4\pi}\frac{e^{-jkr}}{r} Z \int_{F_p} (\vec{s}\times(\vec{s}\times\vec{J}_F(\vec{r}\,'\,)))e^{-jk\vec{s}\cdot\vec{r}\,'}\, df' \ ,$$

and introducing the surface current

$$(2.6) \qquad \vec{J}_F(\vec{r}\,') = \left\{\begin{matrix} 2\vec{n}\times(\vec{e}\times\vec{p}_e)E_e/Z\ e^{-jk\vec{e}\cdot\vec{r}\,'} \\ 0 \end{matrix}\right\} \text{ on the } \left\{\begin{matrix} \text{illuminated} \\ \text{shadowed} \end{matrix}\right\} \text{ parts of the panel.}$$

The geometrical parameters $\vec{r}$, $\vec{r}\,'$, $\vec{e}$, $\vec{s}$, F_p and $\vec{n}$ are explained in Fig. 2.1, while the electric parameters are given by λ = wavelength, $k = 2\pi/\lambda$ = wave number, Z = wave impedance of the propagation medium, $\vec{p}_e = p_x\vec{e}_x + p_y\vec{e}_y$ = unit polarization vector and E_e = magnitude of the incident electric field.

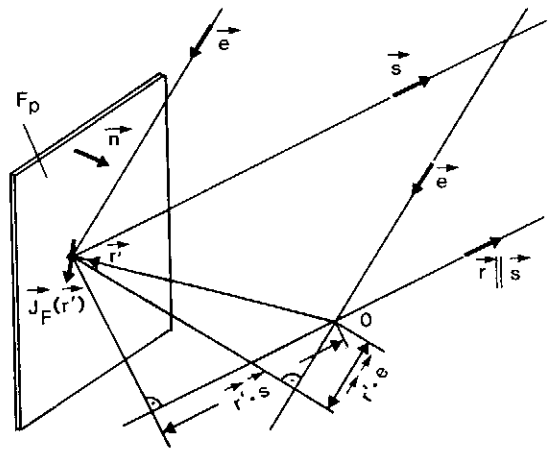

Fig. 2.1
Geometrical scheme for the interpretation of the radiation integral.

The evaluation of the radiation integral for the backscattered ($\vec{e} = -\vec{s}$) field in the observer fixed cartesian coordinate system and the comparison with (2.2) results in the following backscattering matrix:

$$(2.7)\quad [T^{PO}] = -\frac{jk}{2\pi}\frac{e^{-jkr}}{r}\int_{F_p} e^{j2kz'}\,dx'dy'\begin{bmatrix}1 & 0\\ 0 & 1\end{bmatrix}.$$

For a panel of polygonal shape the phase integral can be solved analytically. Details of the integration are given in [4] for panels of triangular and quadrangular shape which are used in the computer program SIG5 to model the target.

Normalizing the scattering matrix to e^{-jkr}/r, the matrix appears purely imaginary. Independent of the orientation of the panel, no differences between xx-polarization and yy-polarization nor any cross-polarization are predicted by PO. This, however, is only true if the panel is perfectly conducting and no double or multiple interactions can occur between pairs or a higher number of panels.

The electric and magnetic fringe currents of Michaeli [9] can be written in a very compact way using the coefficients D_e^f, D_m^f, D_{em}^f (these symbols are proposed by Knott [10]):

$$(2.8)\quad I^f(\psi_e,\psi_s;\beta_e,\beta_s) = -\frac{j2E_{et}}{kZ\sin^2\beta_e}D_e^f(\psi_e,\psi_s;\beta_e,\beta_s) - \frac{j2H_{et}}{k\sin^2\beta_e}D_{em}^f(\psi_e,\psi_s;\beta_e,\beta_s)\ ,$$

$$(2.9)\quad M^f(\psi_e,\psi_s;\beta_e,\beta_s) = \frac{j2ZH_{et}}{k\sin\beta_e\sin\beta_s}D_m^f(\psi_e,\psi_s;\beta_e,\beta_s)\ .$$

$E_{et} = \vec{t}\cdot\vec{E}_e$ or $H_{et} = \vec{t}\cdot\vec{H}_e$ is the component of the incident electric or magnetic field parallel to the edge with unit tangent vector $\vec{t}$. The geometrical parameters ψ_e, ψ_s, β_e, β_s and n are explained in Fig. 2.2. The formulas for D_e^f, D_m^f and D_{em}^f are given in the appendix for the backscattering case ($\psi_e = \psi_s$, $\beta_s = \pi - \beta_e$).

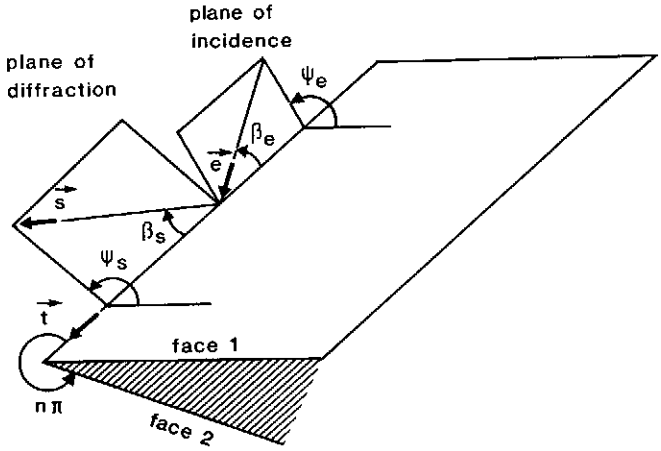

Fig. 2.2
Wedge geometry.

Before choosing the fringe currents of Michaeli, it was necessary to relate this theory to other theories, which, in principle, could be used to solve edge diffraction problems observing the viewpoints given in the introduction.

Though there are several papers [10 - 15] dealing with the relationships between asymptotic diffraction theories, it is useful to summarize the results with the aid of a few statements. Thereby the output of the different theories are given in the form of currents. For mathematical details see [15].

The fringe currents of Michaeli can be written in the following way:

(2.8a) $I^f = I^t - I^{PO}$,

(2.9a) $M^f = M^t - M^{PO}$,

where I^t, M^t are the equivalent electric and magnetic total currents, responsible for the total wedge diffracted field while I^{PO} and M^{PO} are the equivalent PO-components responsible for the PO-field of the wedge. The expressions derived by Michaeli are obtained by asymptotic end-point evaluation of the fringe current radiation integral over the ray coordinate measured along the diffracted ray grazing the surface of the local wedge. The resulting expressions are finite for all aspects of illumination and observation, except for the special case where the direction of observation is the continuation of a glancing incident ray coming from outside the wedge. This situation occurs only in forward scattering.

Choosing the coordinate for the radiation integral in a traditional way normal to the edge, expressions for the fringe currents are obtained [16] which display infinities for certain combinations of observation and incidence directions. These fringe currents are identical to those which can be evaluated [15] from the fringe diffracted fields of Mitzner [7]. Now adapting the fringe currents to the cone of diffracted rays one would expect that these would be identical to those which can be derived from the fringe field expressions of Ufimtsev [6] and which are used in [1]. This is the case for the electric total current, for the magnetic total and PO-current but in general not for the electric PO-current.

The total currents are identical to the filamentary currents of Keller's GTD-field [17], represented by Knott and Senior in a compact manner [18] and denoted as equivalent currents by Ryan and Peters [19] who applied the concept to compute the edge diffracted field in caustic regions. Evaluating the equivalent currents of the GTD for vertical incidence ($\beta_e = 90°$) on a half-plane ($n = 2$) one receives the filamentary currents of the diffracted field derived by Sommerfeld [20].

The difference in the electric PO-currents is given by a coupling term between the incident electric field, being perpendicular to the plane of incidence, and the PO-field having a component parallel to the plane of diffraction. This coupling term is not taken into account by the theory of Ufimtsev as was pointed out in [14]. Only in the case that both faces of the wedge are illuminated by the incident wave does the coupling term become identical to zero [15] and the fringe currents extracted from the theory of Ufimtsev become identical to the fringe currents of Michaeli.

Introducing now the fringe currents (2.8) and (2.9) in the radiation integral over a filamentary current with length L

$$(2.10)\quad \vec{E}_s^f(\vec{r}) = \frac{jk}{2\pi}\frac{e^{-jkr}}{r}\int_L \left(Z\, I^f(\vec{r}')\,(\vec{s}\times(\vec{s}\times\vec{t})) + M^f(\vec{r}')\,(\vec{s}\times\vec{t})\right) e^{jk\vec{s}\cdot\vec{r}'}\, dl' ,$$

one arrives at the backscattering matrix

$$(2.11)\quad [T^f] = -\frac{1}{2\pi}\frac{e^{-jkr}}{r}\int_L e^{j2k\vec{s}\cdot\vec{r}'}\, dl' \times$$

$$\times \begin{bmatrix} D_e^f\, t_x^2 + D_m^f\, t_y^2 - D_{em}^f\, t_x\, t_y & (D_e^f - D_m^f)\, t_x\, t_y + D_{em}^f\, t_x^2 \\ (D_e^f - D_m^f)\, t_x\, t_y - D_{em}^f\, t_y^2 & D_m^f\, t_x^2 + D_e^f\, t_y^2 + D_{em}^f\, t_x\, t_y \end{bmatrix} .$$

The geometrical parameters are explained in Fig. 2.3.

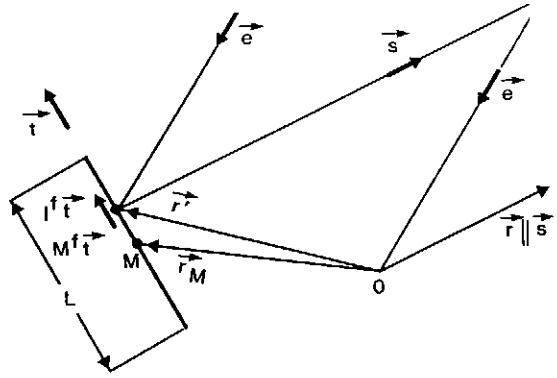

Fig. 2.3
Geometrical sketch to evaluate the radiation integral.

As in the case of the PO-scattering matrix the phase integral can be solved analytically. Introducing the mid-point vector $\vec{r}_M$ of the edge one obtains

$$(2.12)\quad \int_L e^{j2k\vec{s}\cdot\vec{r}'}\, dl' = L\,\frac{\sin(kLt_z)}{kLt_z}\,\frac{e^{j2kr_{Mz}}}{1-t_z^2} ,$$

with $t_z = -\cos\beta_e$.

Normalizing the backscattering matrix $[T^f]$ by e^{-jkr}/r it appears purely real. In general differences between HH- and VV-polarization are predicted. Also, since $[T^f]$ is asymmetric, differences between HV- and VH-polarization are predicted which is not correct for monostatic scattering processes. This is due to corner diffraction effects which arise with an edge of finite length and which are not considered in the theory. Symmetry is observed for the special case of normal wave incidence ($\beta_e = 90°$). Further, if the contour of a panel is a smooth curve, the matrix $[T^f]$ would be symmetric.

For the discussions in the next section, some properties of the coefficients D_e^f, D_m^f, D_{em}^f are needed, which are summarized in the following. Fig. 2.4 shows

the coefficients for normal incidence (β_e = 90°) and a half-plane (n = 2) depending on the angle ψ_e. In Fig. 2.5 the coefficients for a step (n = 1.5) are represented where D^f_{em} is identical to zero. In both cases, mirror symmetries for each coefficient become relevant about ψ_e = 180° for the half-plane and ψ_e = 135° for the step. Further symmetries, now radial symmetries, occur for the half-plane between coefficient D^f_e and D^f_m about ψ_e = 90° and ψ_e = 270°.

Fig. 2.6 shows the coefficients D^f_e, D^f_m and D^f_{em} for ψ_e = 270° and a half-plane now dependent of the angle β_e. One also finds symmetries, namely mirror-symmetry for D^f_e and D^f_m and radial-symmetry for D^f_{em} about β_e = 90°. These symmetries occur for all ψ_e = const.

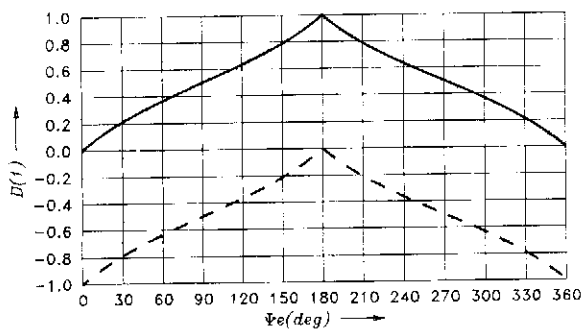

Fig. 2.4
Coefficients D^f_e (——) and D^f_m (---) for a half-plane (n=2) depending on ψ_e; β_e=90°.

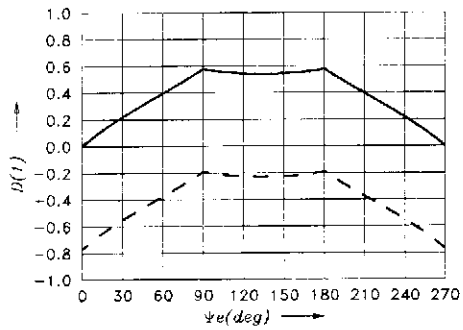

Fig. 2.5
Coefficients D^f_e (——) and D^f_m (---) for a step (n=1.5) depending on ψ_e; β_e=90°.

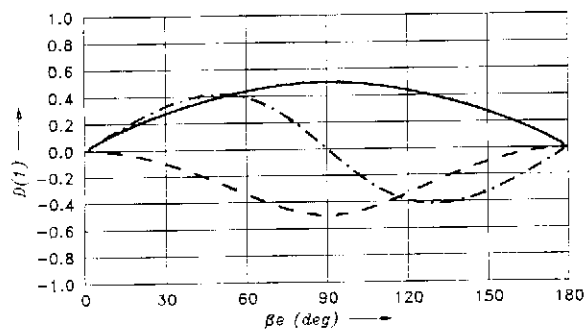

Fig. 2.6
Coefficients D^f_e (——), D^f_m (---) and D^f_{em} (-.-) for a half-plane depending on β_e; ψ_e = 270°.

3. Analysis of the RCS of a Square Test Panel by the PO- and EC-Method

Studies similar to the ones reported here were performed by Ross [21], Sikta, Burnside, Chu and Peters [22], Balanis, Griesser and Marsland [23], Volakis and Ricoy [24], Pelosi, Tiberio, Puccini and Maci [25], Ivrissimtzis and Marhefka [26]. Ross applied the GTD up to triple diffraction to compute the RCS of rectangular flat plates. Sikta et al. used a modified equivalent current concept based on GTD and a corner diffraction analysis to study the RCS of flat plate structures such as a square flat plate, a finlike plate and a disc. Balanis et al. used GTD up to third order diffraction for principal

plane and EC-currents of Michaeli for off-principal plane backscattering of plates. The angular spectrum method along with the generalized matrix formulation were employed for the diffraction analyses of a thick perfectly conducting half-plane by Volakis and Ricoy. Pelosi et al. applied GTD to calculate the RCS of a square plate. Ivrissimtzis and Marhefka used a uniform ray approximation including higher order terms for the analysis of polyhedral structures.

The procedure presented in the previous section is not limited to the simple structure of a flat plate as will be demonstrated in the next section. However, in this section the scattering from a square test plate is investigated in great detail to estimate the efficiency and the limits of application of the chosen method.

The square test panel is analysed at a frequency of 16.66 GHz which results in a wavelength of 17.995 mm. The edge length is 91.4 mm (5.08 λ) and the thickness is 0.8 mm (0.044 λ). In order to have an independent external accuracy check for the following computations, the test panel was chosen to be equal to one of the panels investigated by Ross [21]. The panel is defined in the observer-fixed coordinate system, see Fig. 3.1. The rotations around the x, y and z-axis are defined by the angles φ_x, φ_y, φ_z. An incident wave with electric field vector parallel to the x-axis is designated as horizontally polarized while a field vector parallel to the y-axis describes a vertically polarized field, if the object is rotated around the y-axis for instance.

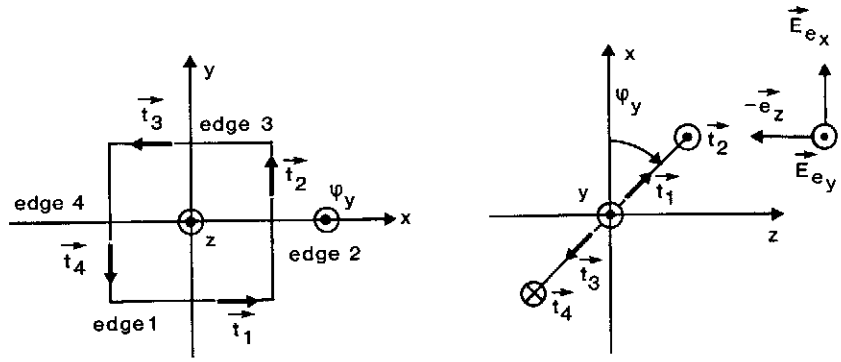

Fig. 3.1 Orientation of the panel in the observer-fixed coordinate system and numbering of the edges for a panel with zero thickness.

Fig. 3.2 resp. Fig. 3.3 shows the experimental RCS-result for horizontal resp. vertical polarization and for the principal plane (φ_x=0, φ_y=α, φ_z=0). For α = 0° one has normal incidence, for α = 90° the panel is seen under grazing incidence. The PO-result for a panel with zero thickness, which is usually compared with experimental results, is shown in Fig. 3.4. The maximum RCS-value amounts to 4.33 dBsm.

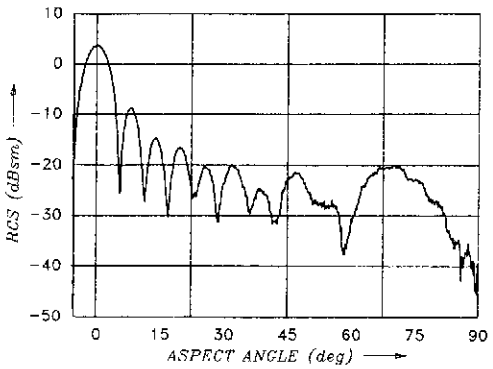

Fig. 3.2
Experimental result for horizontal polarization.

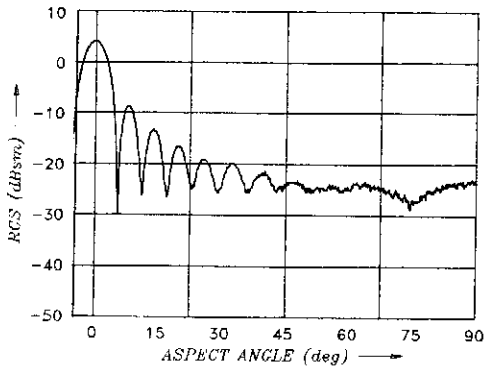

Fig. 3.3
Experimental result for vertical polarization.

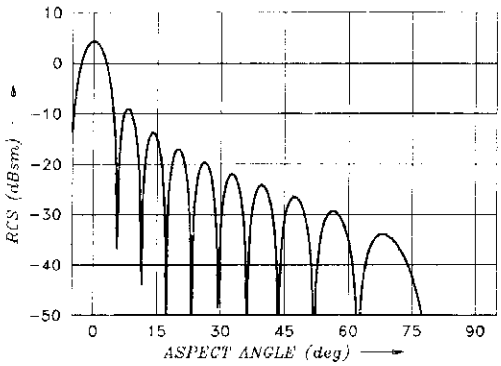

Fig. 3.4
PO-result for the test panel with zero thickness.

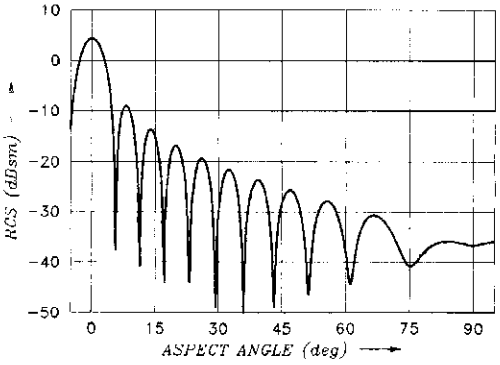

Fig. 3.5
PO-result for the test panel with thickness 0.044 λ.

Besides the smoothing of the deep nulls of the PO-result, the sidelobe peaks far from the mainlobe are significantly higher in the experiment than in the theory. At grazing incidence a deep null of $-\infty$ dB is predicted from theory. In the experiment this null occurs only for horizontal polarization, while for vertical polarization a level of about -27 dB under the main lobe peak can be observed. In view of the experimental results the theoretical results need improvement.

However, it must be emphasized, that for the experiment a panel with a thickness of 0.044 λ was used while for the theory the panel was assumed with zero thickness. Thus far the comparison is a little unfair. If one models the flat plate with the same thickness as was used for the experiment, then it consists of six faces. Each of them can contribute to the total scattered field if it is illuminated by the incident field. The result is presented in Fig. 3.5. One can see that the deep nulls are filled up, that the peaks of the distant sidelobes are higher than in the case of zero thickness, and that, at grazing incidence, an RCS on the order of -41 dB under the peak is predicted compared to $-\infty$ dB for the zero thickness panel and the -27 dB of the experiment.

In the following the influence of the edges is considered. First the panel with zero thickness is analysed.

Edges 2 and 4 make an angle $\beta_e = 90°$ with the incident ray independent from φ_y, see Fig. 3.1, while β_e of edges 1 and 3 varies with $\beta_e = 90° + \varphi_y$. From Eq. (2.11) and Eq. (2.12), one can expect an oscillating behaviour of the RCS of edges 1 and 3 and a monotonic function for edges 2 and 4 with respect to the rotation angle φ_y. For rotation angles $0° < \varphi_y < 180°$, edge 2 is nearer to the radar observer than edge 4, therefore, it is sometimes called the leading edge while edge 4 is the trailing edge.

First the influence of edges 1 and 3 on the RCS computed by PO is considered. The scattering matrix of edge 1 is given by

$$(3.1)\quad [T_1^f] = -\frac{1}{2\pi}\frac{e^{-jkr}}{r} L \frac{\sin(kL\sin\varphi_y)}{kL\sin\varphi_y} \begin{bmatrix} D_e^f & D_{em}^f \\ 0 & D_m^f \end{bmatrix},$$

with arguments $\psi_e = 90°$, $\beta_e = 90° + \varphi_y$ for D_e^f, D_m^f and D_{em}^f. For edge 3 the following formula is obtained:

$$(3.2)\quad [T_3^f] = -\frac{1}{2\pi}\frac{e^{-jkr}}{r} L \frac{\sin(kL\sin\varphi_y)}{kL\sin\varphi_y} \begin{bmatrix} D_e^f & D_{em}^f \\ 0 & D_m^f \end{bmatrix},$$

with $\psi_e = 90°$, $\beta_e = 90° - \varphi_y$.

We can make the following observations:

1. Both scattering matrices are purely real, after normalizing by the factor e^{-jkr}/r.
2. The maximum value is reached for $\varphi_y = 0°$ (the incident ray hits the plate normally). The maximum value amounts to about -32 dBsm which is about -36 dB under the PO-value. This means that the peak value computed by the PO-method is negligibly influenced by the diffraction effects of edges 1 and 3. Since, further, the RCS decreases with increasing angle φ_y in an oscillating manner, both edges have practically no influence on the PO-result.
3. Since mirror symmetries for D_e and D_m hold, see Fig. 2.6, the copolar scattered fields of each edge are equal in amplitude and phase.
4. Both matrices indicate a cross-polarization term and, therefore, are asymmetric. Since, however, for the edge coefficient D_{em}^f a radial symmetry, see Fig. 2.6, holds, the sum matrix $[T_{1,3}^f] = [T_1^f] + [T_3^f]$ is symmetric and is given by

$$(3.3)\quad [T_{13}^f] = -\frac{1}{\pi}\frac{e^{-jkr}}{r} L \frac{\sin(kL\sin\varphi_y)}{kL\sin\varphi_y} \begin{bmatrix} D_e^f & 0 \\ 0 & D_m^f \end{bmatrix},$$

with arguments $\psi_e = 270°$, $\beta_e = 90° - \varphi_y$. The sum matrix predicts differences between horizontal and vertical polarization. However, this effect has practically no influence on the final result.

Fig. 3.6 shows the RCS of edge 1 and 3 for horizontal polarization and Fig. 3.7 for vertical polarization. Fig. 3.8 shows the sum RCS of edges 1 and 3 for horizontal polarization. For vertical polarization only negligible differences exist.

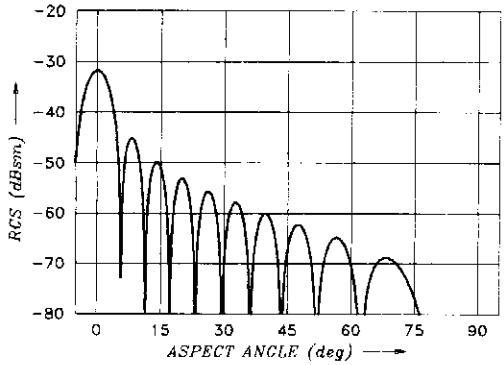

Fig. 3.6
RCS of edge 1 resp. edge 3 for horizontal polarization.

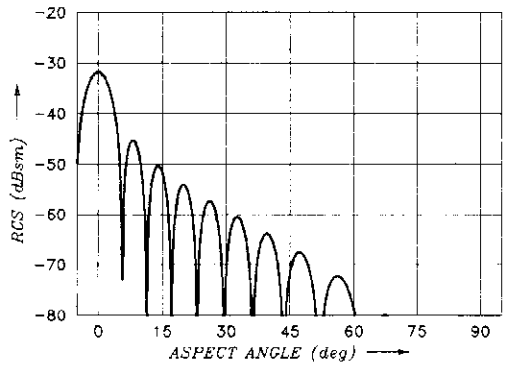

Fig. 3.7
RCS of edge 1 resp. edge 3 for vertical polarization.

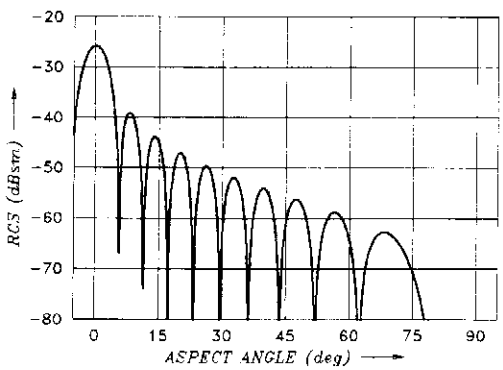

Fig. 3.8
RCS of edges 1 and 3, horizontal polarization.

Contrary to edges 1 and 3, edges 2 and 4 generate contributions of significant practical interest. Bearing in mind that $D^f_{em}(\beta_e = 90°) = 0$, one obtains for edge 2

$$(3.4)\quad [T^f_2] = -\frac{1}{2\pi}\,\frac{e^{-jkr}}{r}\,L\,e^{jka\sin\varphi_y}\begin{bmatrix} D^f_m & 0 \\ 0 & D^f_e \end{bmatrix}.$$

The arguments of the edge coefficients are $\psi_e = 270° - \varphi_y$, $\beta_e = 90°$. For edge 4, we get for the parameters $\psi_e = 270° + \varphi_y$, $\beta_e = 90°$

$$(3.5)\quad [T^f_4] = -\frac{1}{2\pi}\,\frac{e^{-jkr}}{r}\,L\,e^{-jka\sin\varphi_y}\begin{bmatrix} D^f_m & 0 \\ 0 & D^f_e \end{bmatrix}.$$

The following observations can be made:

1. After normalization both scattering matrices appear to be complex.
2. The RCS contributions of both matrices vary monotonically with respect to the rotation angle and are significant compared to the PO-solution.
3. The individual RCS contributions are different from each other and show differences for horizontal and vertical polarization.
4. For horizontal polarization, the contribution of edge 4 dominates, while, for vertical polarization, the contribution of edge 2 dominates.
5. Since symmetry, see Fig. 2.4, is given, the RCS of edge 2 for horizontal (vertical) polarization is identical to the RCS of edge 4 for vertical (horizontal) polarization. For the sum matrix one obtains

$$(3.6)\quad [T^f_{2,4}] = -\frac{1}{2\pi}\frac{e^{-jkr}}{r} L \cos(ka\sin\varphi_y)(D^f_m - D^f_e)\begin{bmatrix}1 & 0\\ 0 & -1\end{bmatrix} - j\frac{1}{2\pi}\frac{e^{-jkr}}{r} L \sin(ka\sin\varphi_y)(D^f_m + D^f_e)\begin{bmatrix}1 & 0\\ 0 & 1\end{bmatrix},$$

where the edge coefficients have the arguments $\psi_e = 270° - \varphi_y$, $\beta_e = 90°$.

The individual RCS contribution of edges 2 and 4 is represented in Fig. 3.9 and Fig. 3.10. The sum RCS of edges 2 and 4 is given in Fig. 3.11.

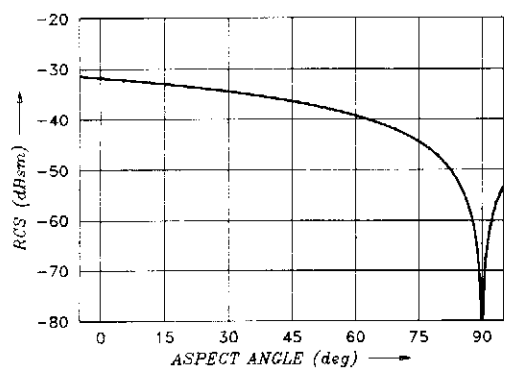

Fig. 3.9
RCS of edge 2 (leading edge) for horizontal polarization and of edge 4 (trailing edge) for vertical polarization.

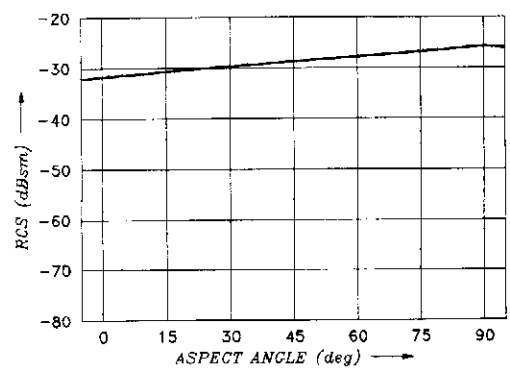

Fig. 3.10
RCS of edge 2 for vertical polarization and of edge 4 for horizontal polarization.

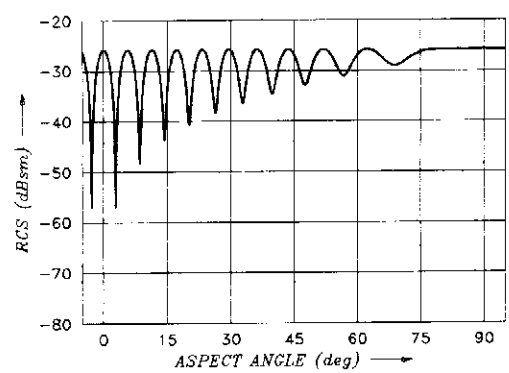

Fig. 3.11
RCS of edges 2 and 4 for both polarizations.

Fig. 3.12 finally shows the PO-result plus the contribution of all four edges which is identical for horizontal and vertical polarization. One can confirm excellent agreement with the experimental results for vertical polarization. It is, however, unsatisfactory that the theoretical solution doesn't indicate any polarization dependence.

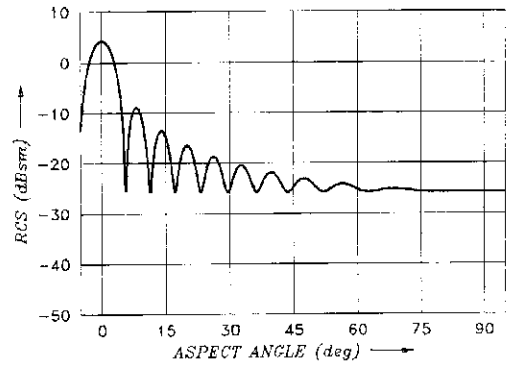

Fig. 3.12
RCS of the test panel with zero thickness for horizontal and vertical polarization computed by PO- and EC-method.

Mathematically this can be explained by discussing the scattering matrix $[T_{2,4}]$. The imaginary part has identical elements for horizontal and vertical polarization. The real part has elements of equal magnitude but opposite sign, so that, with the additive correction of the purely imaginary PO-solution, the matrix behaves like -a-jb for horizontal and +a-jb for vertical polarization. This means that the final RCS result (PO-solution + EC-solution) presents identical values for horizontal and vertical polarization. This is not in agreement with measurements. Physically the effect is explained by the fact that the theory used does not take into account second and higher order diffraction effects. For horizontal polarization, the fields associated with double diffraction e.g. are 4 kL greater than the corresponding vertical polarization contribution [21]. Polarization dependent effects, however, are predicted by the theory for other diagram cuts, other panel shapes (e.g. triangle) or other wedge angles.

The latter is demonstrated for a flat plate with dimensions of the square panel, however, with the same thickness, namely 0.044 λ, as in the experiment. This plate is modeled now by 6 panels and 12 edges (n = 1.5). Without discussion if it is allowed to use the theory for close adjacent edges the result

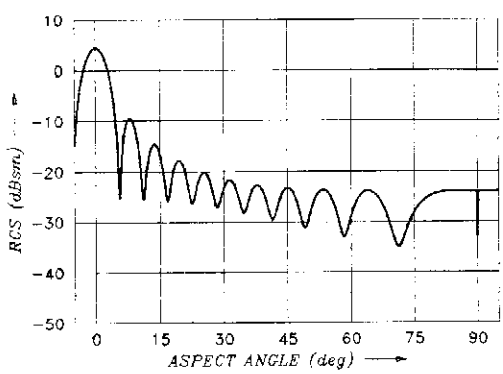

Fig. 3.13
RCS of the test panel with 0.044 λ thickness for horizontal polarization.

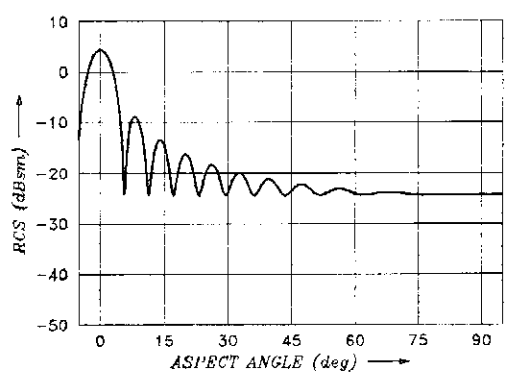

Fig. 3.14
RCS of the test panel with 0.044 λ thickness for vertical polarization.

of the computations is presented in Fig. 3.13 and Fig. 3.14. For horizontal polarization, the discrepancies between theory and experiment have become minor, but the deep null for grazing incidence again is not predicted by the theory.

If the plate is rotated around the z-axis by an angle of $\varphi_z = 45°$ a diagonal cut can be achieved by a following rotation with φ_y. The theoretical results are presented in Figs. 3.15 and 3.16. Again no cross-polarization occurs which is in agreement with symmetrical properties. The experimental results are presented in Figs. 3.17 and 3.18. Since the RCS-values drop very quickly down to levels of about -40 dB under the mainlobe it is not very meaningful to discuss minor deviations between experimental and theoretical results.

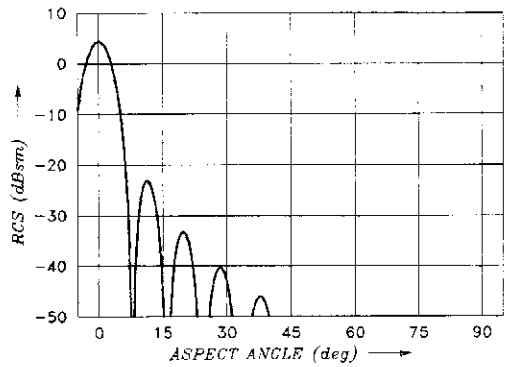

Fig. 3.15
Theoretical RCS of the test panel for a diagonal cut, horizontal polarization.

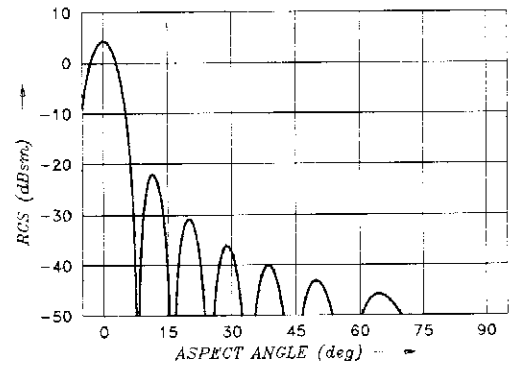

Fig. 3.16
Theoretical RCS of the test panel for a diagonal cut, vertical polarization.

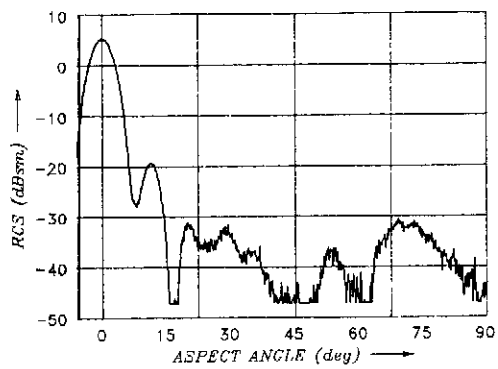

Fig. 3.17
Experimental RCS of the test panel for a diagonal cut, horizontal polarization.

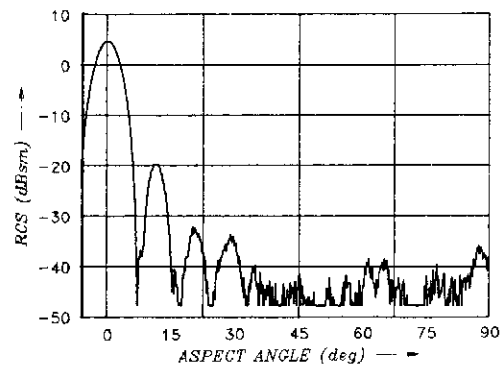

Fig. 3.18
Experimental RCS of the test panel for a diagonal cut, vertical polarization.

Finally, the RCS has been computed for a cut where the rotation axis makes an angle of $\varphi_z = 30°$ with the main axis (15° with the diagonal) of the plate. In this case no symmetry occurs and the theory predicts cross-polarization. Because of the asymmetry in the scattering matrix, the cross-polarization HV, see Fig. 3.19, is slightly different from the cross-polarization VH, see Fig. 3.20. No experiments could be carried out at this time in our institute; see however [27].

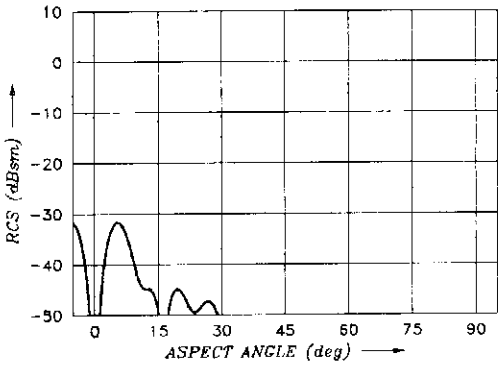

Fig. 3.19
Theoretical RCS of the test panel for a 30°-cut, HV-polarization.

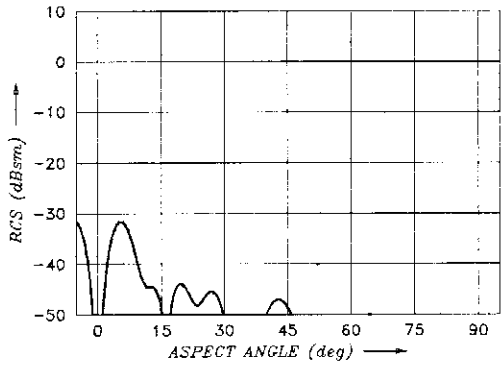

Fig. 3.20
Theoretical RCS of the test panel for a 30°-cut, VH-polarization.

This section is closed with simple formulas derived from the above matrices to estimate the effect of a single edge in relation to the RCS peak value of a panel computed by PO. The panel may be of arbitrary polygonal structure with size A. The edge under consideration has the length L, is hit normally by the incident wave and is rotated around the y-axis by the angle φ_y (this is just the situation of edge 2 in Fig. 3.1). Relating the magnitude of the elements of the scattering matrix given by Eq. (3.4) to the peak value of the PO-scattering matrix, one obtains for horizontal polarization

$$(3.7) \qquad r_{HH} = 20 \log \frac{L\,|D_m^f|}{kA} ,$$

and for vertical polarization

$$(3.8) \qquad r_{VV} = 20 \log \frac{L\,|D_e^f|}{kA} .$$

The arguments of D_m^f, D_e^f are $\psi_e = 270° - \varphi_y$, $\beta_e = 90°$.

Using the values for D_m^f and D_e^f given in Fig. 2.4 for a half-plane (n = 2) and in Fig. 2.5 for a step (n = 1.5), the following table may be established choosing the test panel of this section as an example.

	φ_y	0°	45°	90°	135°	180°	225°	270°
half-plane (n=2)	r_{HH} [dB]	-36.1	-40.8	-∞	-40.8	-36.1	-33.1	-30.1
	r_{VV} [dB]	-36.1	-33.1	-30.1	-33.1	-36.1	-40.8	-∞
step (n=1.5)	r_{HH} [dB]	-32.3	-36.8	-44.5	-42.8	-44.5	-36.8	-32.3
	r_{VV} [dB]	-∞	-40.3	-34.8	-35.4	-34.8	-40.3	-∞

Table 3.1 Level of edge diffraction effects related to the PO-peak value for the square test panel with edge length L=5.08 λ.

4. Application of the EC-Method for a Circular Cylinder and a Double Dihedral

4.1 Circular Cylinder

The test cylinder has a length of 5 λ and a diameter of 1 λ. The wave length is 1128 mm. The broadside RCS amounts to 20 dBsm and the front face RCS to 9.9 dBsm. The cylinder is rotated around an axis vertically to its own axis. Theoretical results for the smooth cylinder based on PTD are published together with experimental results by Ufimtsev in [6]. The circumference of the cylinder was modeled (see Fig. 4.1) by 14 rectangular panels with dimensions 5 λ × 0.22 λ. The deviation from the true cylinder surface was about λ/80. Each of the front faces was modeled with 14 triangles. In the geometrical model artificial edges (n = 1.29) arise between the rectangular panels. The natural circular edges (n = 1.5) between the cylinder circumference and the front faces are approximated by straight lines of length 0.22 λ. Both types of edges are treated in the same way by the theory.

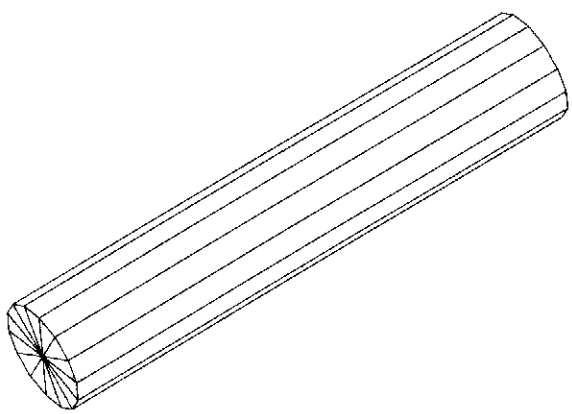

Fig. 4.1
Panel model of the test cylinder.

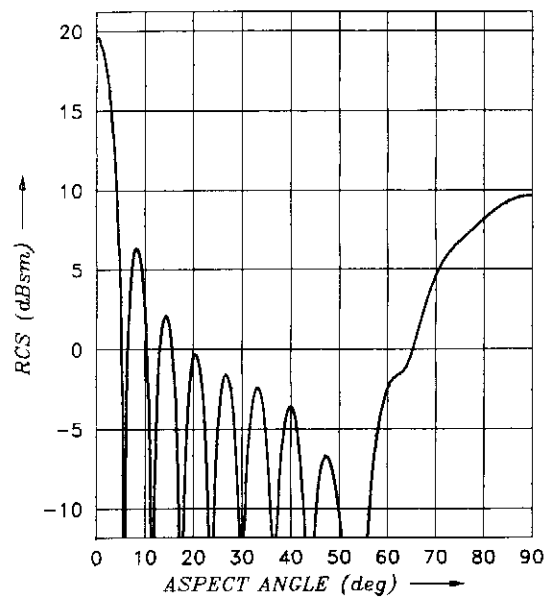

Fig. 4.2
RCS of the clinder modeled by panels, PO-solution.

The PO-solution, insensitive to polarization, is presented in Fig. 4.2. The results of the experiment and of the PTD-theory for horizontal and vertical polarization are given in Fig. 4.3. The broadside peak of the theoretical curves, however, should not exceed 20 dBsm. The pictures of Fig. 4.4, finally present the results of the procedure outlined in this paper. For this special cut they should be identical to the results of Ufimtsev. This is the case except for the difference at broadside incidence and some deviations of minor practical interest.

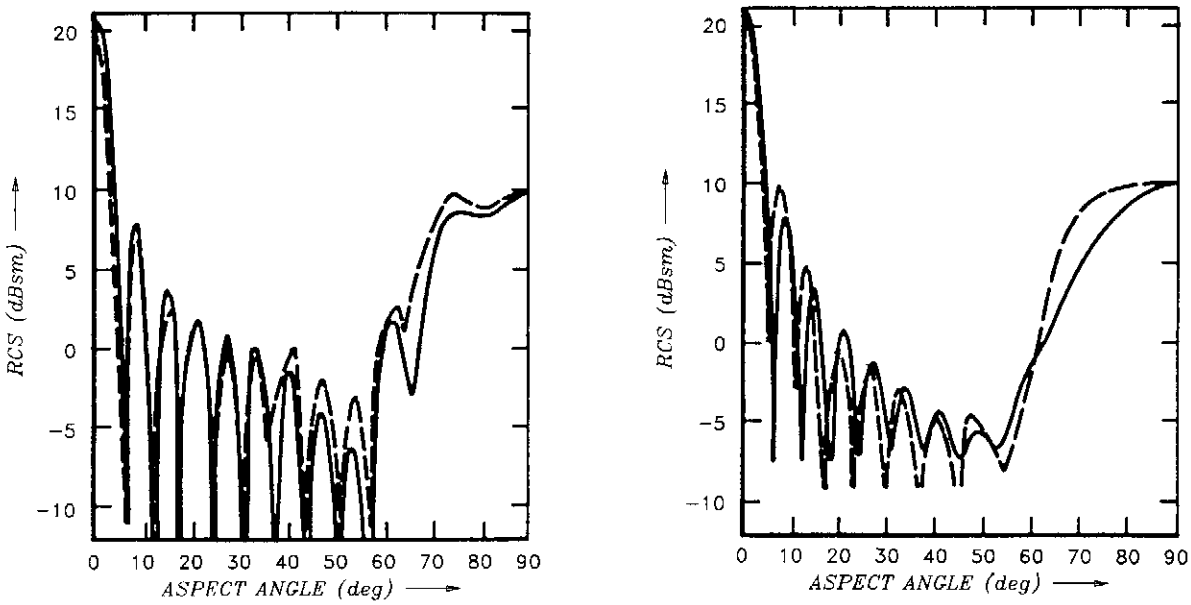

Fig. 4.3 RCS of the smooth cylinder, experiment (---) and PTD-solution (——), left side: HH-polarization, right side: VV-polarization.

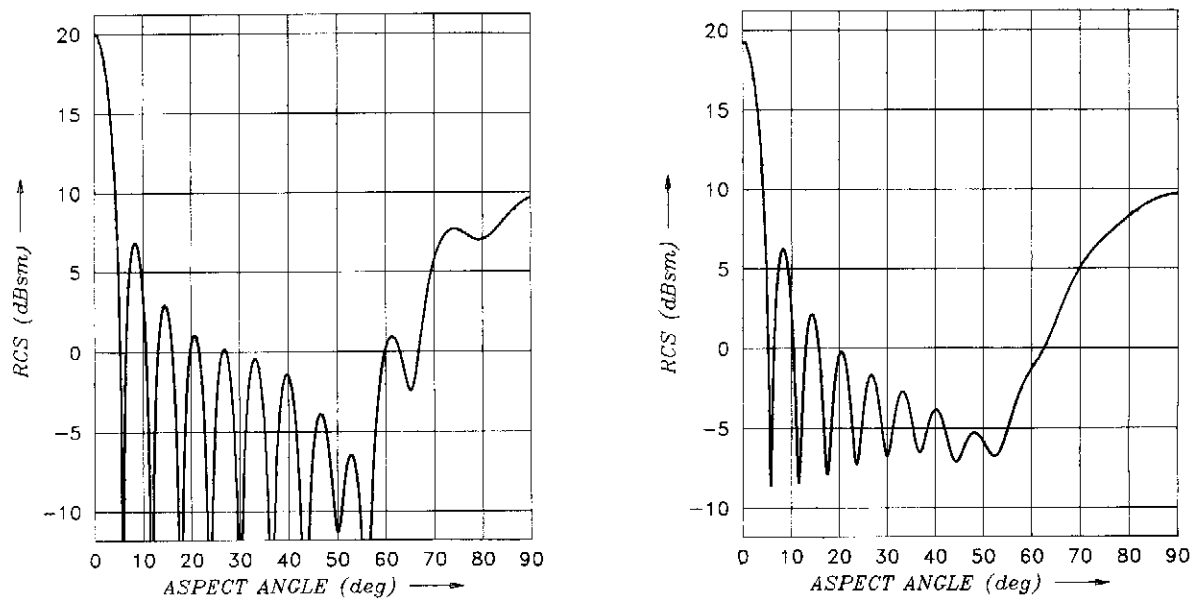

Fig. 4.4 RCS of the cylinder modeled by panels, PO- and EC-solution, left side: HH-polarization, right side: VV-polarization.

4.2 Double Dihedral

A double dihedral constructed on the basis of a cube with additional shadowing surfaces, see Fig. 4.5, is rotated in an unconventional way as shown by Fig. 4.6. For $\alpha = 0°$ the edges of the double dihedral make an angle of 45° with the axis of rotation. The purpose was to generate a strong depolarized backscattered field. Previous PO-results are published for the main cut in [2] and for the diagonal cut within a restricted range of aspect angles in [4].

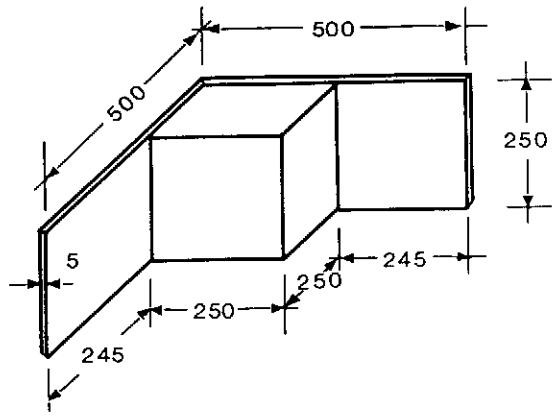

Fig. 4.5
Cube with additional shadowing faces forming a double dihedral, dimensions in mm.

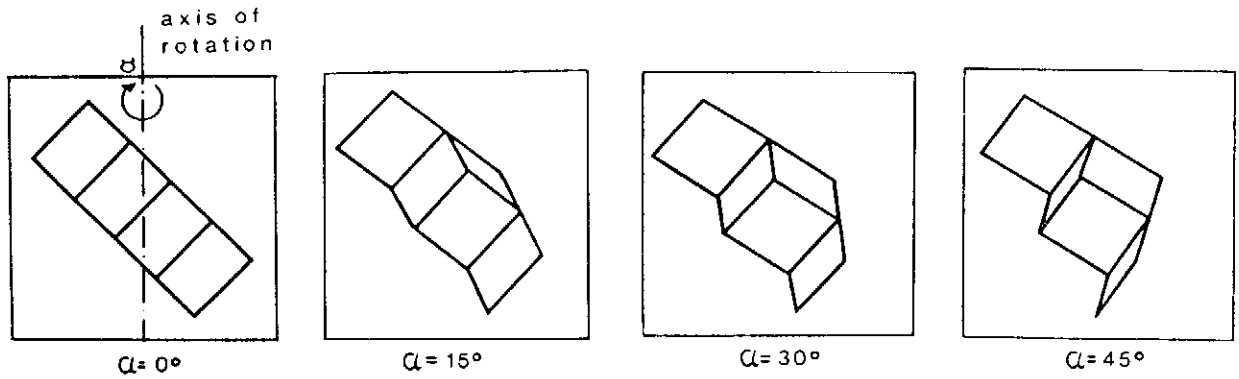

Fig. 4.6 Geometry and axis of rotation.

Figs. 4.7, 4.8 and 4.9 present the results for VH-polarization of experiment, of PO including double reflection and of PO + EC for the full range of aspect angles and a frequency of 15.5 GHz (λ = 19.4 mm). The measurements had to be arranged with great care since a wide dynamic range was needed. In addition, the exact positioning of the double dihedral according Fig. 4.6 caused major problems.

The structure of the pattern around 0° is well represented by PO alone but the decrease is too rapid with increasing aspect angles. In addition, the spikes at -235°, -180°, -125°, -55° and +55° are not predicted by PO. This, however, is the case when the EC-field is added to the PO-field. The spikes, therefore, are due to edge diffraction only.

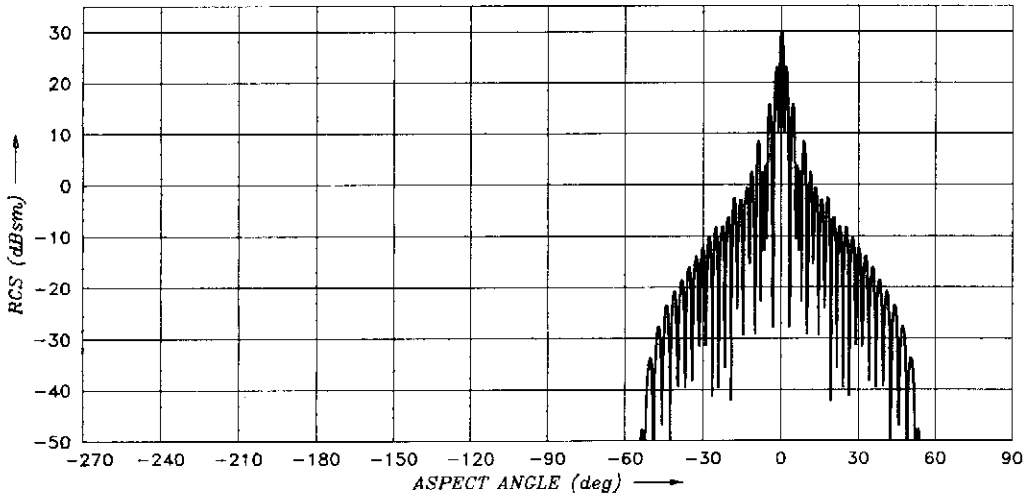

Fig. 4.7 PO-result for the double dihedral, VH-polarization.

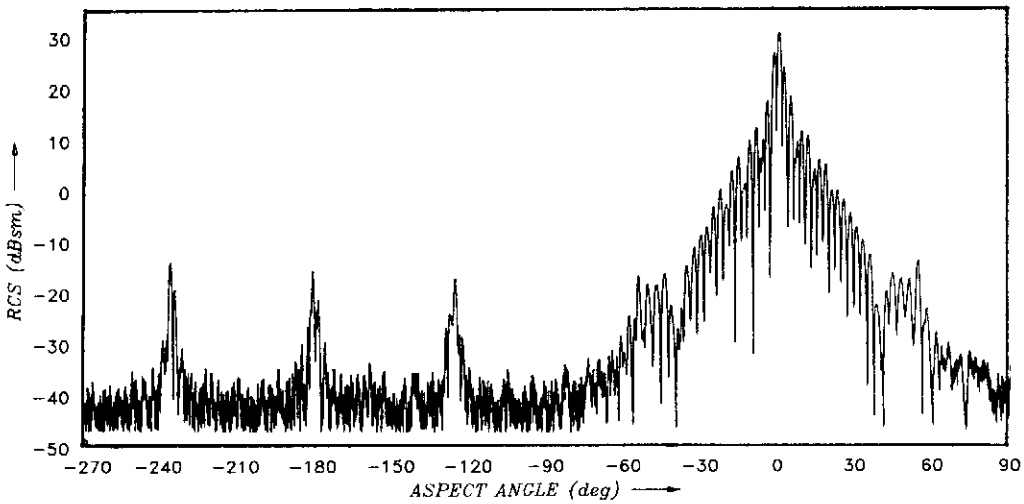

Fig. 4.8 Experimental result.

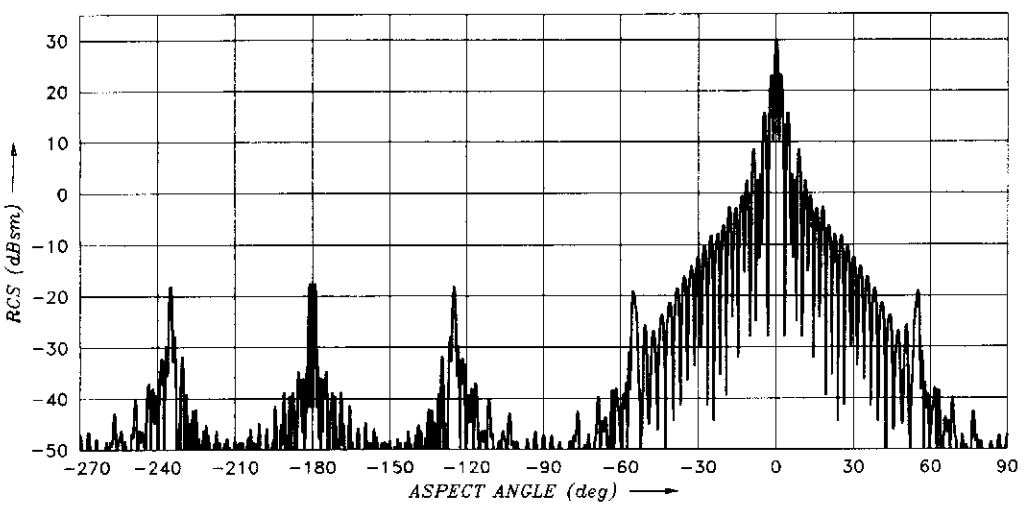

Fig. 4.9 PO- and EC-result.

5. Conclusion

The PO-method is frequently applied with good success to predict the RCS of large and complicated structures modeled by a collection of quadrangular and triangular panels. However, there are certain situations (specific structures, pattern cuts, polarizations) for which a correction of the PO-field by an edge diffracted field is required.

In this paper the concept of equivalent currents (EC) is applied. The fringe currents of Michaeli are used to derive the scattering matrix of an isolated edge with arbitrary length and orientation in an observer fixed coordinate system. The relationship of the method to other theories which are concerned with edge diffraction are summarized by some statements. The theory is applied for the analysis of a square flat plate, of a cylinder and of a double dihedral. All theoretical results are compared with measurements.

The square flat plate with edge length 5.08 λ is analysed in great detail. The results for the principal plane pattern are in excellent agreement for vertical polarization, independent of whether the plate was assumed with zero thickness or with 0.044 λ thickness (as used for the measurements). For horizontal polarization the agreement is unsatisfactory. In the case of zero thickness beyond that identical results for vertical and horizontal polarization are obtained. These effects are due to second order diffraction effects neglected in the EC-theory. This means that further effort is required if one is interested in the improvement of RCS calculations of an isolated plate.

The method is further applied for a cylinder with length 5 λ and diameter 1 λ. The circumference was modeled by 14 rectangular panels, thus introducing artificial edges. Each of the front faces consisted of 14 triangular panels, thus modeling a circular edge by short straight edges. The RCS-results of the EC-method are in good agreement with those of the PTD-method and experiment, both applied for a smooth cylinder.

Finally the concept is used for a double dihedral which was positioned in such a way that strong depolarizations could occur during rotation. Also in this case the correction of the PO-field by the fringe current field was very efficient. The calculated RCS-values are again in good agreement with experimental results.

So one can conclude that the implementation of the presented procedure in a computer program would be efficient enough to treat edge diffraction effects with sufficient accuracy under practical viewpoints.

Acknowledgement

The author thanks Dr. Röde and Dr. K.H. Bethke for the RCS-measurements, Mr. D. Klement for the RCS-computations of the panel with finite thickness and Mrs. M. Malchow for typing the manuscript. Special thanks are expressed to Dr. A. Michaeli whom I was able to contact during the work.

6. References

[1] Youssef, N.N. "Radar Cross Section of Complex Targets". *Proc. IEEE*, Vol. 77, N. 5, May 1989, pp. 722-734.

[2] Klement, D. Preißner, J. Stein, V. "Computation of the Scattering Matrix of Radar Targets: Concept of the Method and First Results". *AGARD-Symposium on Target Signatures*, London, Oct. 1984, CP 364, pp. 20-1 to 20-23, NATO unclassified.

[3] Stein, V. "Physical Optics Method: Prediction of Radar Signatures". *AGARD Lecture Series on Theoretical Aspects of Target Classification*, AGARD-LS-152, 1987.

[4] Klement, D. Preißner, J. Stein, V. "Special Problems in Applying the Physical Optics Method for Backscatter Computations of Complicated Objects". *IEEE Trans. on Ant. and Prop.*, Vol. 36, No. 2, Febr. 1988, pp. 228-237.

[5] Stein, V. "RCS Prediction Models Based on PO and PTD and State of Validation". *AGARD Conference Proceedings 501*, pp. 12-1 to 12-14, 1991.

[6] Ufimtsev, P.Ya. *Method of Edge Waves in the Physical Theory of Diffraction.* Foreign Technology Division, FTD-HC-23-259-71, Translation, AD 733203, Reproduced by National Technical Information Service, Springfield, Va. 22151, 1962.

[7] Mitzner, K.M. *Incremental Length Diffraction Coefficient.* Aircraft Division Northrop Corp., Tech.Rep. No. AFAL-TR-73-296, Apr. 1974.

[8] Chiavetta, J.R. *A Physical Theory of Diffraction for Impedance Wedge.* Boeing Aerospace Co., Doc. D180-26576-1, July 1981.

[9] Michaeli, A. "Elimination of Infinities in Equivalent Edge Currents, Part I: Fringe Current Components". *IEEE Trans. on Ant. and Prop.*, Vol. AP-34, No. 7, July 1986, pp. 912-918.

[10] Knott, E.F. "The Relationship Between Mitzner's ILDC and Michaeli's Equivalent Currents". *IEEE Trans. on Ant. and Prop.*, Vol. AP-33, No. 1, Jan. 1985, pp. 112-114.

[11] Breinbjerg, O.
Rahmat-Samii, Y.
Appel-Hansen, J.
A Theoretical Examination of the Physical Theory of Diffraction and Related Equivalent Currents.
Electromagnetics Institute, Technical University Denmark, Lyngby, R 339, May 1987.

[12] Marhefka, R.J.
Brinkley, T.J.
"Comparison of Methods for Far Zone Scattering from Flat Plate and Cube".
ACES Journal, Fall 1988, Vol. 3, No. 2, pp. 57-78.

[13] Ufimtsev, P.Y.
"Theory of Acoustical Edge Waves".
J. Acoustical Soc. Am., 86(2), Aug. 1989.

[14] Breinbjerg, O.
"Prediction of Bistatic Scattering from Perfectly Conducting Flat Plates by the Method of Equivalent Currents".
1990 URSI Digest, May 7-11, 1990, Dallas, Texas, p. 390.

[15] Stein, V.
Beziehungen zwischen bekannten Theorien zur Behandlung der Beugung an der Kante im Hochfrequenzfall.
DLR-FB 89-49 (1989).

[16] Michaeli, A.
"Equivalent Edge Currents for Arbitrary Aspects of Observation".
IEEE Trans. on Ant. and Prop., Vol. AP-32, No. 3, March 1984, pp. 252-258.

[17] Keller, J.B.
"Geometrical Theory of Diffraction".
Journal of the Optical Society of America, Vol. 52, N. 2, Febr. 1962.

[18] Knott, E.F.
Senior, Th.B.A.
"Comparison of Three High-Frequency Diffraction Techniques".
Proc. IEEE, Vol. 62, No. 11, Nov. 1974, pp. 1468-1473.

[19] Ryan, C.E.
Peters, L., Jr.
"Evaluation of Edge-diffracted Fields Including Equivalent Currents for the Caustic Regions".
IEEE Trans. on Ant. and Prop., Vol. AP-17, pp. 292-299, May 1969.

[20] Sommerfeld, A.
Optik.
Akademische Verlagsgesellschaft, Geest + Portig, Leipzig, 1964, S. 215-238.
see also: "Mathematische Theorie der Diffraction", *Math. Annalen* 4, 1986, S. 317-374.

[21] Ross, R.A.
"Radar Cross Section of Rectangular Flat Plates as a Function of Aspect Angle".
IEEE Trans. on Ant. and Prop., Vol. AP-14, No. 3, 1966, pp. 329-335.

[22] Sikta, F.A.
Burnside, W.D.
Chu, T.T.
Peters, L. jr.
"First-Order Equivalent Current and Corner Diffraction Scattering from Flat Plate Structures".
IEEE Trans. on Ant. and Prop., Vol. AP-31, July 1983, pp. 584-589.

[23] Balanis, C.A.
Griesser, T.
Marsland, D.A.
Electromagnetic Backscattering by Plates and Discs.
Department of Electrical and Computer Engineering, Arizona State University, NASA-CR-180643, 1987.

[24] Volakis, J.L.
Ricoy, M.A.
"Diffraction by a Thick Perfectly Conducting Half-Plane".
IEEE Trans. on Ant. and Prop., Jan. 1987, Vol. AP-35, No. 1, pp. 62-72.

[25] Pelosi, G.
Tiberio, R.
Puccini, S.
Maci, S.
"Applying GTD to Calculations of the RCS of Polygonal Plates".
IEEE Trans. on Ant. and Prop., Vol. AP-38, N. 8, Aug. 1990, pp. 1294-1298.

[26] Ivrissimtzis, L.P.
Marhefka, R.J.
"A Uniform Ray Approximation of the Scattering by Polyhedral Structures Including Higher Order Terms".
IEEE Trans. on Ant. and Prop., accepted for publication.

[27] Young, J.D.
"A Study of Scattering from Edge Waves Using High Resolution Radar Images".
1990 URSI Digest, May 7-11, 1990, Dallas, Texas, p. 49.

Appendix

The coefficients D_e^f, D_m^f, D_{em}^f of the backscattering matrix are given by the theory of Michaeli [9]. For more details see also [15].

$$(A1) \quad D_v^f = D_{1v} - D_{1v}^{po} + D_{2v} - D_{2v}^{po} \ , \ v = e,m,em \ ,$$

$$(A2) \quad D_{1e} = \frac{\sin\frac{\psi_e}{n}}{n} \frac{1}{\cos\frac{\pi-\alpha_1}{n} - \cos\frac{\psi_e}{n}} \ ,$$

$$(A3) \quad D_{1m} = \frac{\sin\psi_e}{n} \frac{\sin\frac{\pi-\alpha_1}{n}}{\sin\alpha_1} \frac{1}{\cos\frac{\pi-\alpha_1}{n} - \cos\frac{\psi_e}{n}} \ ,$$

$$(A4)\quad D_{1em} = \frac{1}{n}\cos\beta_e\,(\mu_1 + \cos\psi_e)\,\frac{\sin\frac{\pi-\alpha_1}{n}}{\sin\alpha_1}\,\frac{1}{\cos\frac{\pi-\alpha_1}{n} - \cos\frac{\psi_e}{n}}\,,$$

$$(A5)\quad D_{1e}^{po} = -\,U(\pi-\psi_e)\,\frac{\sin\psi_e}{\mu_1 + \cos\psi_e}\,,$$

$$(A6)\quad D_{1m}^{po} = D_{1e}^{po}\,,$$

$$(A7)\quad D_{1em}^{po} = 0\,.$$

$$(A8)\quad \mu_1 = \cos\psi_e - \frac{2}{\tan^2\beta_e}\,,$$

$$(A9)\quad \alpha_1 = \arccos\mu_1\,,$$

$$(A10)\quad U(x) = \left\{\begin{matrix}1\\0\end{matrix}\right\} \quad \text{for} \quad \left\{\begin{matrix}x > 0\,,\\ x < 0\,.\end{matrix}\right.$$

The coefficients D_{2v}, D_{2v}^{po} result from D_{1v}, D_{1v}^{po} by the following transformations:

$$(A11)\quad \psi_e \to n\pi-\psi_e\,, \qquad \beta_e \to \pi-\beta_e\,.$$